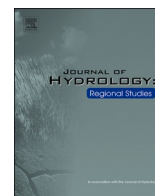




ELSEVIER

Contents lists available at ScienceDirect

Journal of Hydrology: Regional Studies

journal homepage: www.elsevier.com/locate/ejrh

Impact of meteorological conditions on water resources in the Upper East Region of Ghana using remotely-sensed and modelled hydrological data

C.I. Kelly^{a,1}, C.M. Hancock^{b,2}, S. Grebby^{c,3}, S. Marsh^{c,4}, V.G. Ferreira^{d,5},
N.A.S. Hamm^{a,*,6}

^a Geospatial and Geohazards Research Group, Faculty of Science and Engineering, University of Nottingham Ningbo China, Ningbo, China

^b School of Architecture, Building and Civil Engineering, Loughborough University, Loughborough, UK

^c Nottingham Geospatial Institute, Faculty of Engineering, University of Nottingham, Nottingham, UK

^d School of Earth Sciences and Engineering, Hohai University, Nanjing, China

ARTICLE INFO

Keywords:

GRACE

Evapotranspiration

Water storage

Precipitation

Ghana's Upper East Region

Water budget

ABSTRACT

Study region: The Upper East Region, Ghana, West Africa, lies within the Volta Basin, floods annually, and contributes substantially to Ghana's food production.

Study focus: We assessed precipitation (P), evapotranspiration (ET), and total water storage anomalies from GRACE (TWSA) and GLDAS-Noah (TWCA) to study the influence of the UER's climate on water availability between 2002 and 2017. We analysed (1) the relative uncertainties of the data sets using the triple-cornered hat method, (2) the terrestrial water budget to validate TWSA/TWCA and (3) cross- and multi-correlation analyses to study the relationship between water storage (or availability) and meteorological variables.

New hydrological insights: We found strong correlations between the different P products ($r > 0.96$), between the different GRACE products ($r > 0.95$), but not between the different ET products. The hybrid P , TWSA from the Jet Propulsion Laboratory, and ET from ERA-5 had the smallest relative uncertainties. TWSA increased by $9.8 \pm 0.8 \text{ mm yr}^{-1}$ while TWCA decreased. P and ET showed no evidence of a trend and were similarly influenced by the other meteorological variables. However, 93 of 183 months had water surplus and mean net P was positive – indicating the UER received more water than it lost. These agree with the increasing TWSA trend. The water budget validation also confirmed that GRACE can be used for water management; GLDAS-Noah underestimates storage in the UER.

* Corresponding author.

E-mail addresses: calebaid2000@gmail.com (C.I. Kelly), nicholas.hamm@nottingham.edu.cn (N.A.S. Hamm).

¹ <https://orcid.org/0000-0002-3292-8271>.

² <https://orcid.org/0000-0002-9692-0439>.

³ <https://orcid.org/0000-0001-9768-2682>.

⁴ <https://orcid.org/0000-0002-1168-6760>.

⁵ <https://orcid.org/0000-0003-2209-9921>.

⁶ <https://orcid.org/0000-0002-5105-7846>.

<https://doi.org/10.1016/j.ejrh.2022.101124>

Received 28 January 2022; Received in revised form 26 May 2022; Accepted 27 May 2022

Available online 2 June 2022

2214-5818/© 2022 Published by Elsevier B.V. This is an open access article under the CC BY-NC-ND license (<http://creativecommons.org/licenses/by-nc-nd/4.0/>).

1. Introduction

The 2020 World Meteorological Organization's report on the state of the global climate showed that temporal variations in climate indicators and extreme weather events, e.g., droughts and floods, increased in 2020 in comparison to previous years (World Meteorological Organization, 2020). A consequence is the continual rise in temperatures, the effect of which is pronounced over vulnerable regions such as West Africa, where increasing temperatures are linked to the large climatic variability, particularly in terms of rainfall (Christensen et al., 2013). Since the region depends heavily on agriculture, it is critical to understand the impact of climate variability on water resources.

In situ data for water resources monitoring are typically unavailable or scanty over areas such as Ghana's Upper East Region (UER). The UER (1) contributes substantially to Ghana's food production (Owusu et al., 2013), (2) has a long dry season and (3) gets flooded annually – a result of rainfall and the opening of the Bagre dam in Burkina Faso (e.g., Bempah and Oyhus, 2017). The region's strategic location explains the decision of the Government of Ghana to construct a multi-purpose dam to (1) mitigate the effects of flooding, (2) aid irrigation and, (3) provide electricity (Ghana Web, 2021). These necessitate the study of water resources in the region for sustainable crop production. Yet, according to the Ghana Meteorological Agency, there are only six weather stations distributed across the UER. Hydrological data are either unavailable or not easily accessible. Although the UER falls entirely within the Volta Basin, which has been the subject of some hydrological studies (Andam-Akorful et al., 2015; Ni et al., 2017), the basin spans several jurisdictions with varying climates. Consequently, basin-wide analysis of hydro-meteorological data may not represent processes in the UER. However, the sparseness or unavailability of in situ components of total water storage (TWS) presents a huge limitation to water resources analysis in the UER.

Satellite and global hydro-meteorological data provide an alternative to monitor water resources. Examples include satellite-only, gauge-only and hybrid precipitation (P) products and evapotranspiration (ET) products. For hydrological studies, modelled data such as those from the Global Land Data Assimilation System (GLDAS) (Rodell et al., 2004b) may provide adequate hydrological information over an area (Syed et al., 2008). Also, the advent of the Gravity Recovery and Climate Experiment (GRACE) mission has enabled the measurement of TWS anomalies (TWSA) by recovering temporal variations in the Earth's gravity field at monthly scales (Wahr et al., 1998, 2004). Thus, GRACE data are applicable to studying the temporal evolution of the different drivers of the water cycle – P , ET , etc. (Chen et al., 2010; Landerer et al., 2020; Ramillien et al., 2006). In this study, we assessed various freely available hydro-meteorological and GRACE products to study water resources in the data-poor UER. We used methods including the three-cornered hat (TCH) for a relative uncertainty estimation of the respective data sets to enable the selection of the most appropriate of the analysed data. While such methods yield relative rather than absolute uncertainties, they are widely used as proxies to absolute error analysis and provide sufficient information to support data selection in data-poor regions/situations (Ferreira et al., 2016; Galindo and Palacio, 2003; Gray and Allan, 1974; McColl et al., 2014; Yakubu et al., 2019).

A potential limitation to our study is the resolution of GRACE. The robustness of GRACE measurements cannot be assured because the area of the UER ($\sim 8600 \text{ km}^2$) is substantially smaller than $150,000 \text{ km}^2$ (Longuevergne et al., 2013; Rowlands et al., 2005). This leads to the mixing of GRACE signals in the UER with the surrounding signals, which can cause biases if the surrounding signals have different signs (e.g., Vishwakarma et al., 2018). However, if storage variations in the UER are $> 8 \text{ km}^3$, this will improve the signal-to-noise ratio (SNR) of the recovered signals (Tourian et al., 2015). Thus, GRACE may provide accurate TWSA in the UER. GRACE studies have been conducted over similarly smaller regions (Biancamaria et al., 2019; Guo et al., 2016; Ni et al., 2017; Tourian et al., 2015) including one as small as 38 km^2 (Zheng et al., 2018). Even so, validating GRACE over a small region, especially one with no prior GRACE studies, is necessary to inspire confidence in the results. Where available and sufficient, in situ data may be used to validate GRACE. Here, we used the water budget equation to evaluate whether GRACE is suitable for the UER. GRACE can provide TWS change (TWSC). Hence, we expect that the difference of net precipitation and GRACE TWSC will provide insight into the validity of GRACE results over the UER. This assertion is supported, for instance, by Riegger et al. (2012) who mentioned that the water budget equation can be used to estimate errors in GRACE. Furthermore, the combination of GRACE and fluxes in the water budget equation is well-established in the literature (Abolafia-Rosenzweig et al., 2021; Andam-Akorful et al., 2015; Rodell et al., 2004a).

Previous studies over the UER focused on the spatial-temporal variations of only a single aspect of the region's climate such as rainfall or temperature. For instance, rainfall reportedly decreased between 1954 and 2014, while temperatures increased (Issahaku et al., 2016). Quaye-Ballard et al. (2020a) also showed that more than 50 % of the UER was characterised by a decrease in rainfall between 1981 and 2016. Owusu et al. (2013) reported severe desertification, a drought indicator, in the UER. Yet, how these and other hydro-meteorological conditions impact water availability in the UER has yet to be studied. Given the agroecological importance of the UER to Ghana (Owusu et al., 2013), understanding the relationship between hydro-meteorological processes and water availability is necessary to implement policies for water resources management. Hence, our study extended the scope of previous studies by analysing multiple hydro-meteorological variables in relation to water resources. Our objectives were: (1) to assess freely available space geodetic, hydro-meteorological, and modelled hydrological data in the UER, (2) to assess the use of GRACE over the UER and (3) extend the scope of previous UER studies to characterise the impact of multiple hydrological and meteorological variables on water resources. Our study is important because it provides pertinent information that can be used by stakeholders such as the Hydrological Services Department, the Ghana Water Company Limited, and the Ghanaian Ministry of Food and Agriculture. The findings of this study will also provide important information to the authorities of the yet-to-be-constructed Pwalugu Dam on its operations (e.g., on irrigation).

2. Regional setting

2.1. Geography

The UER shares boundaries with two of Ghana's neighbouring countries: Togo to the east and Burkina Faso to the north. It is located at 10.2–11.2° N, 1.6° W to 0.03° E in the northeast of Ghana (Fig. 1). The area is approximately 8600 km², making up about 4 % of Ghana and 2 % of the Volta Basin. It is characterised by a fairly undulating topography with moderate variations (Kelly et al., 2021). Slopes range between 1 % and 5 %, but with a few outcrops and highlands (Ghana Statistical Service, 2014). The maximum elevation is 455 m and the minimum is 119 m, with the majority lying around 200 m. The major occupation of the region is agriculture (Ministry of Food and Agriculture, 2019) and farmers typically rely on ponds and dugouts for irrigated farming during the dry season (Quaye-Ballard et al., 2020b). The region is drained by the Sisili River and the Red and White Volta Rivers. Furthermore, the region's valleys are characterised by heavy textured soils, making them suitable for rice farming. However, some of the soils are composed of coarse material, e.g., gravel, stones, and concretion, thus reducing their water retention capabilities (Ministry of Food and Agriculture, 2019). The vegetation of the UER is Savannah, mainly Guinea-Savannah, but also Sudan-Savannah (Ministry of Food and Agriculture, 2019).

2.2. Climatology

The UER is characterised by two meteorological regimes: the rainy (April to October) and the dry (November to March) seasons. The dry season lasts relatively longer than the rainy season (6–7 months vs 5–6 months) and is characterised by low humidity and dry winds (harmattan). Dry season average temperatures range between 15 °C (December–February) and 45 °C (March–April), with relatively lower nighttime temperatures. The mean annual rainfall in the region is 921 mm, but exceeded 1200 mm in 2002 and 2007 (Ministry of Food and Agriculture, 2019). Although rainfall in the region is decreasing (Quaye-Ballard et al., 2020a; Yiran and Stringer, 2016), the region is inundated annually. These floods occur in response to contributions from the Bagre Dam in Burkina Faso, rainfall, and the Volta river.

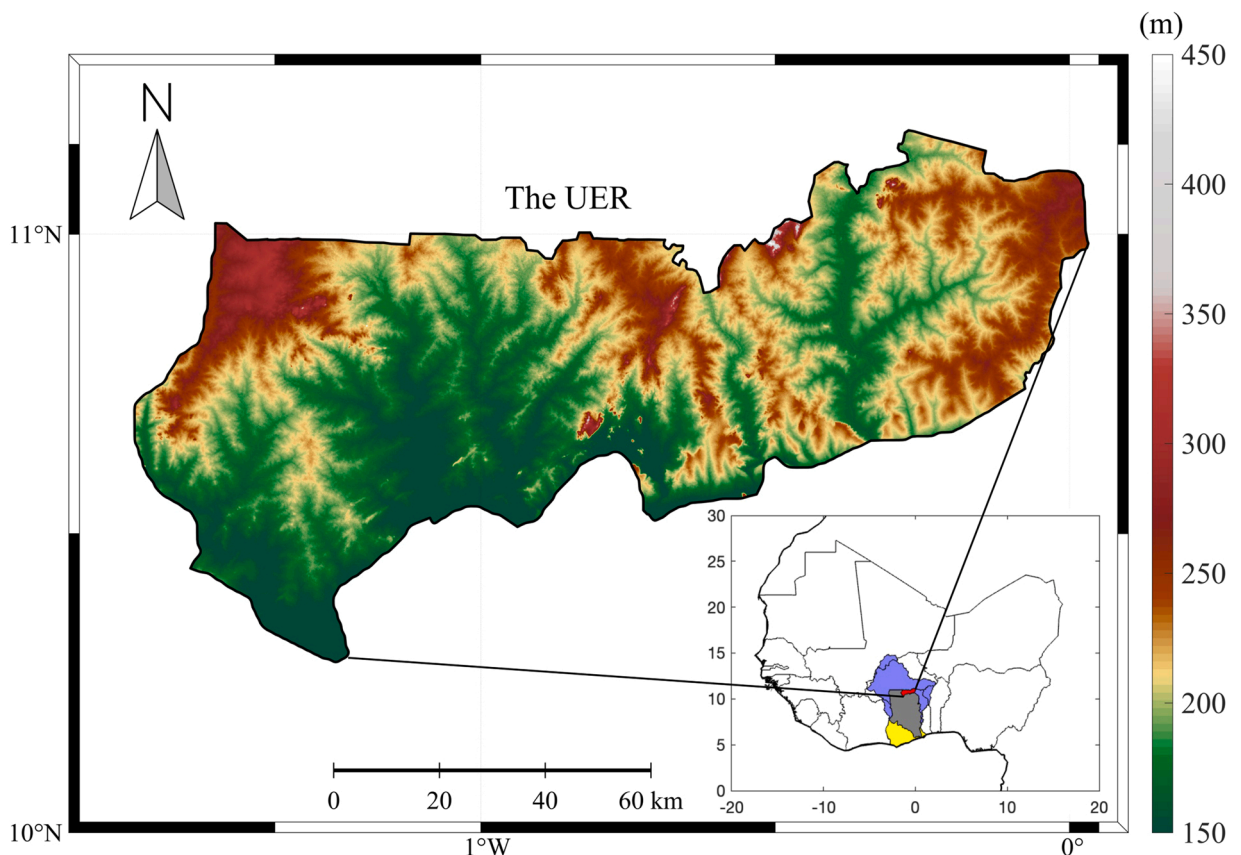


Fig. 1. Topography of the UER. The area is about 8600 km², making up approximately 4 % of the total area of Ghana and 2 % of the Volta Basin. The inset map shows the location of UER (red) in Ghana and the locations of Ghana (yellow) and the Volta Basin (purple) in West Africa.

3. Material and methods

Fig. 2 summarises the main data and processing workflow adopted in our study. We used water storage, rainfall (P), evapotranspiration (ET), and meteorological data. Methods include (1) areal averaging for time series extraction, (2) multi-linear regression for time series decomposition and, (3) cross-correlation and, (4) multiple correlation analyses, both, to examine the relationship between different variables.

3.1. Data sets

The data sets are summarised in Table 1 and are described in detail as follows.

3.1.1. GRACE TWSA products

We used the mass concentration (mascon) solutions release 6 version 2 from the Jet Propulsion Laboratory (JPL) and the Center for Space Research (CSR) at the University of Texas (Save et al., 2016; Save, 2020; Wiese et al., 2019). For comparison with the mascon grids, we also used GRACE TELLUS land mass grids that were calculated from CSR RL05 (CSR-T) spherical harmonic coefficients (SHCs) (Landerer, 2020). We applied the gain factors that were provided with the JPL mascon (JPL-M) and CSR-T solutions to restore the attenuated signals and reduce leakage effect. GRACE signal attenuation and leakage occur during JPL mascon processing and post-processing of SHCs (CSR-T). Restoring signals and reducing the leakage effect improves the signal-to-noise ratio (SNR) of GRACE-derived TWSA (Landerer and Swenson, 2012; Wiese et al., 2016). CSR-M is distributed on a 0.25° grid, JPL-M on a 0.5° grid, and CSR-T is distributed on a 1° grid. TWSA represents total water storage as anomalies from the 2004 to 2009 mean. The long-term mean is subtracted to account for the static gravity field.

The study period was limited to April 2002–June 2017 mainly because of the almost 1-year gap between the two GRACE missions. There is also the possibility of a bias between the two missions, which requires further investigation (not addressed here). Apart from Section 4.4, we used cubic spline interpolation to fill in missing GRACE months (cf. Andam-Akorful et al., 2015; Ramillien et al., 2006). This was necessary for the implementation of Eq. (3), which describes storage change from month to month (Ramillien et al., 2006).

3.1.2. The Global Land Data Assimilation System (GLDAS)

GLDAS uses satellite and terrestrial data as constraints to land surface states to provide an array of (near) global, high-resolution, and accurate land surface models (Rodell et al., 2004b). We calculated total water content (TWC) from GLDAS-Noah (Rui et al., 2018) as the sum of canopy water storage (CWS) and soil moisture storage (SMS). Then we converted TWC into anomalies (TWCA) by estimating and subtracting the mean for the period 2004–2009, consistent with the GRACE solutions. We chose GLDAS-Noah to evaluate the influence of unmodelled storage compartments in GLDAS for storage analysis in the UER.

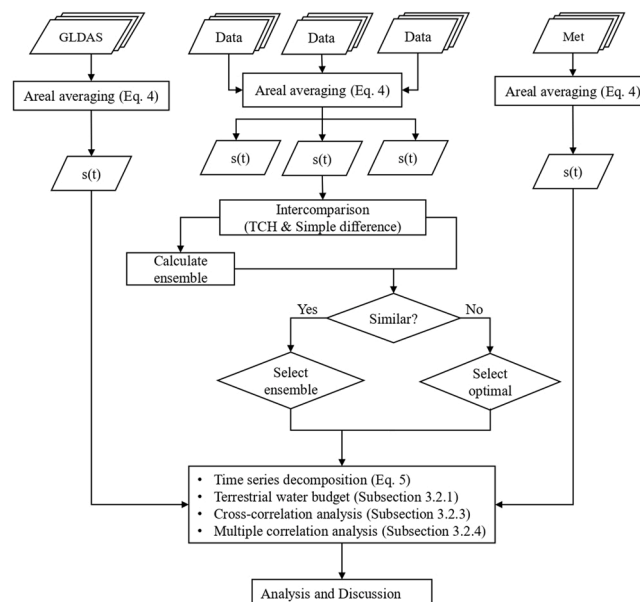


Fig. 2. Flow chart summarising the main methods in this study. TCH is the three-cornered hat (TCH) method. “Met” is used to describe meteorological data sets described in Section 3.1.6. “Data” represents the three solutions of water storage, ET , and P . $s(t)$ is the area-weighted average of the data sets (Eq. (4)).

Table 1
Summary of data sets used in this study.

| Data | Quantity | Resolution | Website | Last accessed | |
|----------------------|---|------------|---------|---|------------|
| CSR Mascon RL06v02 | TWSA | Monthly | 0.25° | http://www2.csr.utexas.edu/grace | 2021-08-06 |
| CSR TELLUS land grid | TWSA | Monthly | 1° | https://podaac.jpl.nasa.gov/GRACE | 2021-08-06 |
| JPL Mascon RL06v02 | TWSA | Monthly | 1° | https://podaac.jpl.nasa.gov/GRACE | 2021-08-06 |
| GLDAS-Noah v2.1 | TWCA, temperature, humidity, wind speed, pressure, SWR, <i>ET</i> | Monthly | 0.25° | https://disc.gsfc.nasa.gov/ | 2021-01-01 |
| CRU TS v4.04 | PET | Monthly | 0.5° | https://crudata.uea.ac.uk/cru/data/hrq/ | 2021-04-16 |
| ERA-5 | <i>ET</i> | Monthly | 0.1° | https://cds.climate.copernicus.eu/cdsapp#!/dataset/reanalysis-era5-land-monthly-means?tab=form | 2021-01-29 |
| MODIS (MOD16A2) | <i>ET</i> | 8 days | 500 m | https://modis.gsfc.nasa.gov/data/dataproduct/mod16.php | 2021-01-18 |
| CHIRPS | <i>P</i> | Monthly | 0.05° | https://data.chc.ucsb.edu | 2020-12-10 |
| GPM | <i>P</i> | Monthly | 0.1° | https://disc.gsfc.nasa.gov | 2021-01-01 |
| CPC | <i>P</i> | Daily | 0.125° | https://psl.noaa.gov | 2020-07-06 |

3.1.3. Precipitation

We did not have access to ground-based precipitation data. Thus, we compared three freely available precipitation (*P*) products: the Global Precipitation Measurement (GPM), the Climate Prediction Centre (CPC), and the Climate Hazards group Infra-red Precipitation with Stations (CHIRPS). These products represent satellite-only, gauge-only, and hybrid (satellite and gauge) solutions and are described as follows.

The GPM mission is a collaboration between NASA and the Japan Aerospace Exploration Agency and comprises a constellation of satellites providing continuity to global precipitation measurement from the Tropical Rainfall Measuring Mission (TRMM) (Hou et al., 2014). We used the satellite-only IMERG Final Precipitation L3 version 6 product, which has spatial and temporal resolutions of 0.1° and 1 month.

The CPC solution is a purely gauge-based global rainfall solution using data from more than 30,000 stations 0.125° grid (Xie et al., 2007, 2010). It is managed by the Physical Sciences Laboratory of the US's National Oceanic and Atmospheric Administration distributed at spatial and temporal resolutions of 0.5° and 1 day.

The CHIRPS product is managed by the Climate Hazards Centre of the University of California and is based on a combination of rain gauge and satellite data. We used the monthly CHIRPS version 2 (v2.0) product distributed on 0.05° grid (Funk et al., 2015).

3.1.4. Evapotranspiration

Evapotranspiration (*ET*) fluxes were extracted from three hydrological models: GLDAS-Noah, the Moderate Resolution Imaging Spectroradiometer (MODIS), and the fifth generation reanalysis for the global climate and weather (ERA-5) from the European Center for Medium-Range Weather Forecasts.

The MODIS *ET* algorithm (MOD16) combines a surface energy partitioning process and environmental factors that impact *ET* to calculate a global 8-day *ET* product using data from MODIS, onboard the Aqua and Terra satellite, and station-based meteorological observations (Mu et al., 2007, 2011). We downloaded the 500-m, 8-day resolution MOD16A2 product and aggregated to monthly *ET*. The data is provided in the Sinusoidal map projection. Hence, we dumped the latitude and longitude using the eosdump software (<http://hdfEOS.org/software/eosdump.php>; last accessed: January 20, 2021).

ERA-5 is the replacement of the third generation ERA-Interim reanalysis and leverages developments in the Integrated Forecasting System Cycle version 41r2 (Hersbach et al., 2018). We downloaded the ERA5-Land monthly averaged reanalysis data and calculated *ET* as the sum of evaporation and vegetation transpiration. The data is provided on a 0.1° grid. Quantities in ERA-5 are provided relative to the first day of the month. Thus, we calculated monthly estimates by multiplying these quantities by the number of days in each month.

3.1.5. Aridity

Aridity describes the unavailability of water within a region. This dryness is described by the aridity index (*AI*) given by Cherlet et al. (2018):

Table 2
Aridity index and classification (Cherlet et al., 2018).

| Classification | <i>AI</i> |
|----------------|--------------------|
| Hyperarid | $AI < 0.05$ |
| Arid | $0.05 < AI < 0.20$ |
| Semi-arid | $0.20 < AI < 0.50$ |
| Dry sub-humid | $0.50 < AI < 0.65$ |
| Humid | $AI \geq 0.65$ |

$$AI = \frac{P}{PET}, \quad (1)$$

where P is the annual average of precipitation and PET is the annual average of potential evapotranspiration. AI classifications are summarised in Table 2 (Cherlet et al., 2018).

To avoid the possible biasing of AI analysis because of the incomplete years in our study (start and end years respectively April 2002 and June 2017), we recalculated AI from 2003 to 2016. For PET , we used monthly CRU Time Series version 4.04 (CRU TS v4.04) (Harris et al., 2020). CRU TS v4.04 is managed by the Climate Research Unit (CRU) of the University of East Anglia.

3.1.6. Other meteorological data

In addition to P and ET , we used temperature, wind speed, humidity, and net short wave radiation (SWR) flux, all extracted from GLDAS-Noah. We refer to these collectively as predictor variables and analysed their impact on TWSA, rainfall, ET , and available water.

3.2. Methods

3.2.1. The UER water budget

The terrestrial water budget equation relates water storage in an area to P , runoff (Q) and ET , and is expressed as (Brutsaert, 2005; Ramillien et al., 2006):

$$P - ET - Q - \frac{ds}{dt} = 0, \quad (2)$$

where $\Delta s = ds/dt$ is TWS change (TWSC) or TWC change (TWCC), and describes storage change from month to month.

The terrestrial water budget equation balances if there are no errors in the individual data sets, presenting a means of a mutual validation of the data. Thus, we used Eq. (2) to validate GRACE and GLDAS-Noah estimates of Δs . We approximated Δs by numerically differentiating GRACE/GLDAS-Noah storage anomalies using the central difference formula:

$$\Delta s(t) \approx \frac{s(t+1) - s(t-1)}{2}, \quad 2 \leq t \leq t_{max} - 1, \quad (3)$$

where t is time (mth).

We also filtered P and ET using a 300-km half-width Gaussian filter (Wahr et al., 1998) to account for the spectral inconsistencies between GRACE and P and ET (Ferreira and Zibrila, 2015).

3.2.2. Time series analysis

For time series, we extracted grid points (x) falling within the UER and calculated their area-weighted average, $s(t)$:

$$s(t) = \frac{\sum_{i=1}^n a_i x_i(t)}{\sum_{i=1}^n a_i}, \quad (4)$$

where n is the number of pixels and a represents the area per pixel. We resampled all data sets on a 0.25° grid to match that of CSR-M. For GRACE, we calculated equivalent water volume (EWW, km^3) by multiplying equivalent water height (EWH, mm) by a_i .

We adopted a time-variable regression model to analyse $s(t)$. We fitted the harmonic function characterised by an offset, a linear trend, annual and semi-annual amplitudes and phases (Ogawa et al., 2011):

$$s(t) = \beta_0 + \beta_1 \Delta t + \sum_{k=1}^2 A_k \cos(\omega k t - \phi_k) + \epsilon, \quad (5)$$

to $s(t)$. The regression coefficients, β_0 and β_1 denote the constant term and the linear trend, respectively, and A and ϕ are respectively the amplitude and phase. Δt is the time difference between each data point (in years) and the median time of the study (2009.5) and $\omega = 2\pi/T$ is the angular frequency, with the period $T = 1 \text{ yr} = 365.25$ days. k has a value of 1 or 2 respectively corresponding to the annual and semi-annual terms. To solve for the parameters and their standard errors, we expanded the last term into two pairs of sine and cosine functions; a pair for each value of k . The expansion uses the trigonometric identity that $\cos(\omega k t - \phi_k) = B_k \cos(\omega k t) + C_k \sin(\omega k t)$. We then estimated the parameters, β_0 , β_1 , B_k , and C_k and their standard errors via a least squares inversion. Then, $A_k = \sqrt{B_k^2 + C_k^2}$ and $\phi_k = \tan^{-1}\left(\frac{C_k}{B_k}\right)$.

We evaluated the estimated parameters by testing the null hypothesis that the parameter was equal to zero against the alternative that it was not equal to zero using the t -test. We calculated t as the ratio of the parameter estimates to their respective standard errors (Kutner et al., 2005), from which the associated p -values were calculated using the tcdf function in MATLAB R2021a.

3.2.3. Uncertainty analysis

Since we did not have in situ data, for the different groups of data sets (i.e., TWSA, P , and ET), we calculated the relative uncertainties (σ_{TCH}) of the three solutions in each group using the generalised three-cornered hat (TCH) method (Galindo and Palacio, 2003; Gray and Allan, 1974; Premoli and Tavella, 1993; Tavella and Premoli, 1994). The TCH method allowed us to estimate the relative error variances of the three time series, with the underlying assumption of a normal distribution of their errors. Like the extended triple collocation (ETC) method (McCull et al., 2014), TCH does not require a reference data set (Gray and Allan, 1974). However, we chose TCH because ETC has the strict requirement that the error variances of the systems must be uncorrelated. The error variances of our data sets are likely correlated (cf. Yakubu et al., 2019), thus excluding the use of ETC in our study. We refer the interested reader to Ferreira et al. (2016) and the references therein for further details on the TCH technique.

We used σ_{TCH} to calculate the ensemble averages of the different groups using a weighted averaging method similar to Eq. (4) by replacing a_i with $1/\sigma_{TCH}$ and $x_i(t)$ with $s(t)$. We then used the ensemble average to estimate the relative biases of the solutions. We calculated the bias as the difference of the individual products and the ensemble average. All results based on TCH should be interpreted relative to the input solutions. For instance, if solution A has the smallest σ_{TCH} of the solutions A, B, and C, we will refer to it as the best of the three. However, this conclusion is true only in the context of the three solutions. We also expect that solutions with smaller σ_{TCH} will have the least deviation (bias) from their ensemble average. This is because solutions with larger σ_{TCH} will be down weighted in the ensemble average. In some cases, we also calculated the SNR of the different solutions as the ratio of the mean of the time series and σ_{TCH} . For decomposed time series components (Eq. (5)), we used the estimated standard errors from the least squares inversion (Section 3.2.2).

3.2.4. Cross-correlation analysis

Given two random, equal-length (L) time series X and Y acquired at times $t = 1, 2, \dots, L$, cross-correlation analysis examines the relationship between X and Y at different times. If the variables are detrended, then this is given by the cross-covariance of X and Y (Chatfield and King, 2019):

$$\text{cov}(X_t, Y_{t+l}) = E[(X_t - \mu_X)(Y_{t+l} - \mu_Y)] = \sigma_{XY}(l), \quad (6)$$

where $l = \text{lag}$ (in mth). The cross-covariance is related to the cross-correlation, r_{XY} , by:

$$r_{XY}(l) = \frac{\sigma_{XY}(l)}{\sigma_X \sigma_Y}, \quad (7)$$

where σ_X and σ_Y are the standard deviations of X and Y . We estimated $r_{XY}(l)$ by shifting Y to the right and left of X and each time calculating the Pearson's correlation coefficient. We determined the lag at which r_{XY} was maximum. This represents the lag (time) of maximum dependence between X and Y . If maximum r_{XY} occurs anywhere else but lag 0, then there is a time delay (phase shift) between X and Y . If $r_{XY} > 0$ or $r_{XY} < 0$, then X leads or lags Y at the given lag. We also calculated the square of Eq. (7), i.e., the coefficient of determination, R^2 , to determine the percentage of variations in the response variable that are accounted for by the predictor variable.

3.2.5. Multiple correlation coefficient

We used multiple correlation analysis to inspect the relationship between the predictor variables (Section 3.1.6) and the other quantities. For this, we formed two matrices – the $N \times 1$ vector \mathbf{b} representing the response variable and the $N \times (J + 1)$ matrix \mathbf{A} of the predictor variables. We set the first column of \mathbf{A} to 1 (Abdi, 2007) and solved for the J unknowns, $\hat{\mathbf{b}}$, via a least squares inversion.

The multiple $R_{Y,1,\dots,J}^2$, which describes the percentage of variations in the response variable that can be explained by the predictor variables, was then calculated as:

$$R_{Y,1,\dots,J}^2 = \frac{SSR}{SST}, \quad (8)$$

where SSR is the regression sum of squares and is given by:

$$SSR = \hat{\mathbf{b}}^T \mathbf{A}^T \mathbf{b} - \frac{1}{N} (\mathbf{1}^T \mathbf{b})^2 \quad (9)$$

and SST is the total sum of squares, given by:

$$SST = \mathbf{b}^T \mathbf{b} - \frac{1}{N} (\mathbf{1}^T \mathbf{b})^2, \quad (10)$$

where $\mathbf{1}$ is a column vector of ones and represents the first column of \mathbf{A} and $(\cdot)^T$ denotes the transpose operator.

4. Results

In line with the aim and objectives of the study, we used the following results to answer the questions (1) what is the relative performances of $ET/P/TWSA$ solutions from different providers over the UER? (2) Can GRACE provide TWSA over the UER with a high

SNR? (3) How does GLDAS-Noah perform over the UER? and (4) What is the relationship between meteorological conditions and water availability in the UER?

The results for the time series analysis are shown in Table 3. This shows the parameter estimates ($\hat{\beta}_0$, $\hat{\beta}_1$, \hat{A}_1 , \hat{A}_2 , $\hat{\phi}_1$ and $\hat{\phi}_2$) from Eq. (5) and their associated standard errors. In most cases the standard errors are small compared to the point estimates of the parameters, indicating that the parameter is clearly significantly different from zero. This is a particular concern for the estimate of the trend, $\hat{\beta}_1$. If this parameter is not significantly different from zero (p-value < 0.05), it indicates that there is no evidence of a trend over time and this component can be ignored in the model.

4.1. Rainfall

Fig. 3 shows the time series of rainfall (Eq. (4)) from GPM, CPC, CHIRPS, and their ensemble average. Table 4 summarises their statistics differences, and relative uncertainties. The rainfall peaks usually occur in August and the maximum occurred in August 2007 for all the products (Table 4 and Fig. 3).

Fig. 3 and Table 4 indicate good agreement between the three rainfall products. The products also had high correlation coefficients ($r > 0.96$, p-value < 0.001), and their estimated parameters from Eq. (5) (not shown) were similar. Relative to their ensemble average, CHIRPS and CPC underestimated rainfall (negative biases, Table 4), while GPM overestimated rainfall. We selected the CHIRPS P product for the rest of the study because of its relatively low bias (Table 4) and σ_{TCH} . See Table 3 for the estimated parameters of CHIRPS.

4.2. Aridity

We illustrate the aridity PET time series in Fig. 4a. We used PET to calculate aridity index (AI). The AI (Eq. (1)) for the period April 2002 to June 2017 ranged between 0.4 and 0.75 (Fig. 4b), i.e., between semi-arid and humid (Table 2) (Cherlet et al., 2018). When we excluded the incomplete years (2002 and 2017) and recalculated AI, the average was 0.64, that is, a dry sub-humid classification (Table 2). This classification suggests the UER is susceptible to dryness.

4.3. Water loss

The results for runoff (not shown) did not exceed 2 mm mth⁻¹ and were, therefore, excluded from the analysis of water loss. Fig. 5 shows the ET time series, and Table 5 summarises their differences, biases, and relative uncertainties. Unlike the P products, the ET solutions were more dissimilar. For instance, MOD16A2 did not exceed 80 mm mth⁻¹, but GLDAS-Noah and ERA-5 exceeded 100 mm mth⁻¹. The r ranged between 0.76 (p-value < 0.001, MOD16A2 and GLDAS-Noah) and 0.91 (p-value < 0.001, ERA-5 and GLDAS-Noah), indicating a comparatively wider variability in the estimation of ET by these solutions.

We selected ERA-5 as the best of the three solutions. The maximum ET flux from ERA-5 occurred in October 2015 and the minimum occurred in March 2006. The time series of the ERA-5 ET product showed no evidence of a trend (Table 3).

4.4. Inter-comparison of GRACE solutions

We found good agreement between the three GRACE solutions (Table 6, Fig. 6). The minimum correlation coefficient was greater than 0.95 (p-value < 0.001). Table 6 shows the summary statistics along with their biases and relative uncertainties and Fig. 6 shows their time series along with the ensemble average. We selected the JPL-M solution for the rest of our analyses.

Table 3

Harmonic analysis of quantities showing the dimensionless constant term, the linear trend (mm yr⁻¹), the amplitudes (mm) and phases (°), and their standard errors. The standard errors are written in parentheses. ()^f denotes filtered P – ET. ()* represents 0.02 < p-value < 0.05, ()⁺ represents p-value >> 0.05, ()[#] represents p-value = 0.07, and ()^o represents p-value = 0.04. All other parameters had p-value < 0.001.

| Quantity | $\hat{\beta}_0$ | $\hat{\beta}_1$ (mm yr ⁻¹) | Amplitude (mm) | | Phase (°) | |
|-----------------------|------------------------|---|----------------|-------------|----------------|------------------------|
| | | | \hat{A}_1 | \hat{A}_2 | $\hat{\phi}_1$ | $\hat{\phi}_2$ |
| TWSA | 34.3 (3.3) | 9.8 (0.8) | 117.0 (4.7) | 10.2 (2.3) | 37.5 (4.7) | 13.9 (7.2) |
| TWCA | -6.7 (1.8) | -2.2 (0.4) | 80.1 (2.6) | 15.3 (1.9) | 27.3 (2.6) | 9.8 (5.5) |
| P | 81.0 (2.4) | 0.01 (0.6) ⁺ | 108.8 (3.5) | 19.9 (1.8) | 37.7 (3.4) | 3.3 (5.2) ⁺ |
| ET | 59.1 (0.9) | 0.3 (0.2) [#] | 53.0 (1.3) | 16.9 (1.4) | 13.2 (1.3) | 12.2 (5.7)* |
| P – ET | 22.0 (2.6) | -0.3 (0.6) ⁺ | 66.3 (3.6) | 20.7 (3.1) | 38.3 (3.6) | 4.2 (5.4) ⁺ |
| TWSC | 1.0 (1.6) ⁺ | -0.03 (0.4) ⁺ | 58.3 (2.3) | 20.0 (2.2) | 33.4 (2.3) | 3.9 (3.9) ⁺ |
| TWCC | 0.4 (1.1) ⁺ | 0.06 (0.3) ⁺ | 40.7 (1.6) | 23.5 (2.3) | 24.2 (1.6) | 3.0 (3.8) ⁺ |
| (P – ET) ^f | 11.7 (1.0) | -0.4 (0.2) ^o | 70.1 (1.5) | 20.3 (1.2) | 18.2 (1.5) | 12.6 (4.6) |

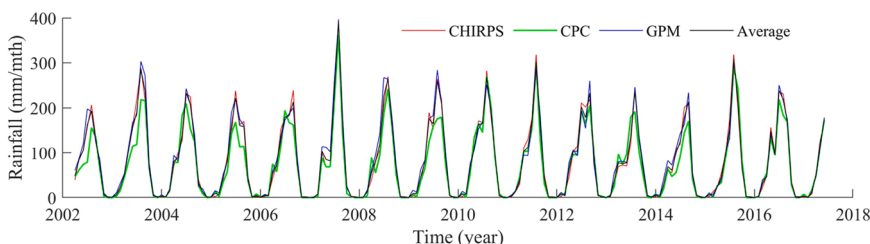


Fig. 3. Areal-averaged rainfall time series over the UER estimated from CHIRPS (red curve), CPC (green curve), and GPM (blue curve). The black curve represents the ensemble average of CHIRPS, CPC, and GPM.

Table 4

Summary statistics of the rainfall solutions and their TCH-based relative uncertainties (σ_{TCH}). We calculated the bias as the mean of the difference between each solution and the ensemble average. Units: mm/mth; Mean and Bias: mm.

| Solution | Min | Max | STD | Mean | Bias | σ_{TCH} |
|--------------|--------|--------|-------|-------|-------|----------------|
| GPM | 0.03 | 393.97 | 87.23 | 84.12 | 3.36 | 12.4 |
| CPC | 0 | 362.87 | 76.95 | 71.85 | -8.92 | 20.4 |
| CHIRPS | 0.57 | 396.88 | 87.14 | 80.71 | -0.06 | 11.1 |
| Ensemble | 0.28 | 390.96 | 85.12 | 80.77 | | |
| GPM - CPC | -44.66 | 118.74 | 23.85 | 12.28 | | |
| GPM - CHIRPS | -47.25 | 61.46 | 16.62 | 3.42 | | |
| CPC - CHIRPS | -98.79 | 58.15 | 23.22 | -8.86 | | |

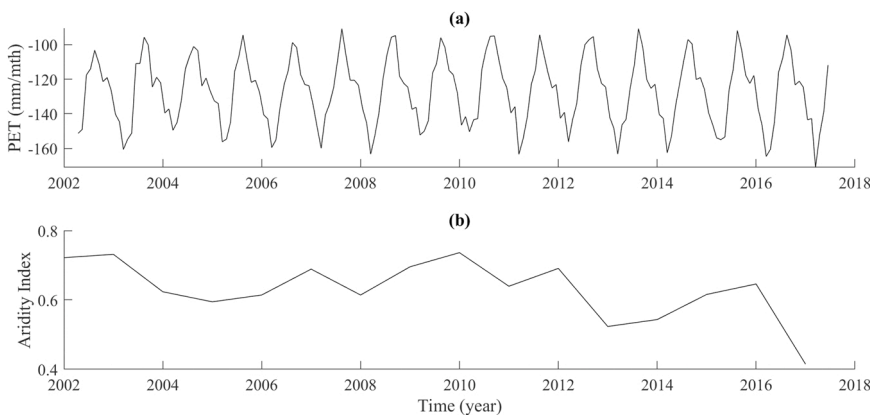


Fig. 4. Time series of (a) potential evapotranspiration from CRU TS v4.04 and (b) aridity index.

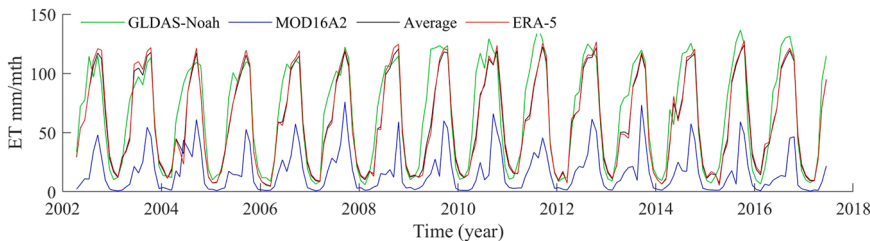


Fig. 5. Evapotranspiration from MOD16A2 (blue), GLDAS-Noah (green), ERA-5 (red), and the ensemble average (black).

4.5. Terrestrial Water Storage (TWS) anomalies from GRACE

We recalculated monthly areal averages from the JPL-M data from April 2002 to June 2017. Fig. 7 shows the time series of TWSA expressed in EWH (red) and EWV (green). The minimum anomaly (-161.1 mm, -50.7 km³) was recorded in May 2006 and the maximum (290.4 mm, 91.3 km³) was recorded in October 2012. We summarised the time series components of TWSA (EWH) in

Table 5

Summary statistics of the ET solutions and their relative uncertainties. We calculated the bias as the mean of the difference between each solution and the ensemble average. Units: mm/mth; Mean and Bias: mm.

| Solution | Min | Max | STD | Mean | Bias | σ_{TCH} |
|----------------------|--------|--------|-------|-------|--------|----------------|
| ERA-5 | 4.5 | 127.63 | 40.37 | 58.74 | 1.01 | 6.08 |
| MOD16A2 | 0.49 | 75.90 | 17.96 | 16.95 | -40.79 | 27.25 |
| GLDAS-Noah | 5.96 | 138.05 | 43.09 | 65.16 | 7.43 | 16.36 |
| Ensemble | 4.92 | 123.95 | 39.23 | 57.74 | | |
| ERA-5 - GLDAS-Noah | -71.52 | 29.90 | 17.46 | -6.42 | | |
| ERA-5 - MOD16A2 | -20.41 | 109.13 | 27.92 | 41.80 | | |
| GLDAS-Noah - MOD16A2 | 4.82 | 120.40 | 31.78 | 48.22 | | |

Table 6

Summary statistics of the GRACE solutions. We calculated the bias as the mean of the difference between each solution and the ensemble average. Units: mm/mth; Mean and Bias: mm.

| Solution | Min | Max | STD | Mean | Bias | σ_{TCH} |
|---------------|---------|--------|--------|--------|-------|----------------|
| JPL-M | -161.06 | 282.56 | 104.49 | 27.44 | 3.85 | 13.8 |
| CSR-M | -150.81 | 222.34 | 83.64 | 16.13 | -7.45 | 28.2 |
| CSR-T | -203.43 | 314.24 | 121.82 | 28.09 | 4.50 | 34.8 |
| Ensemble | -174.32 | 274.85 | 103.66 | 23.59 | | |
| JPL-M - CSR-M | -59.17 | 93.58 | 31.38 | 11.30 | | |
| JPL-M - CSR-T | -81.50 | 107.24 | 37.51 | -0.65 | | |
| CSR-M - CSR-T | -105.78 | 74.12 | 44.84 | -11.95 | | |

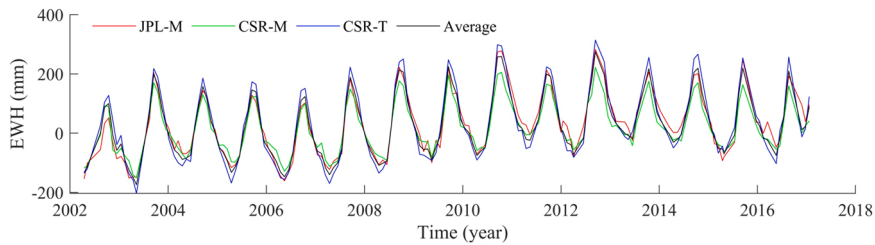


Fig. 6. TWSA expressed in terms of equivalent water height (EWH) for JPL mascon (red), CSR mascon (green), and CSR TELLUS (blue) from April 2002 to January 2017.

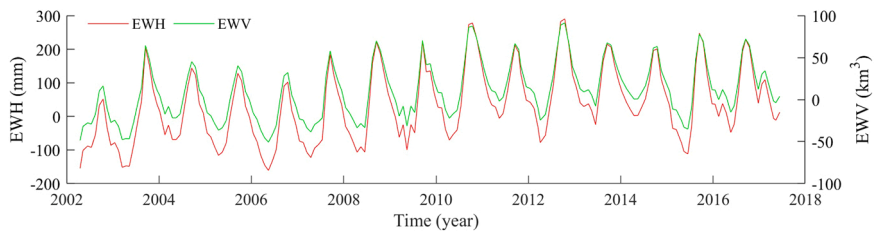


Fig. 7. TWSA time series over the UER. Red curve represents TWSA expressed in terms of EWH (mm) and green denotes equivalent water volume of TWSA (km³).

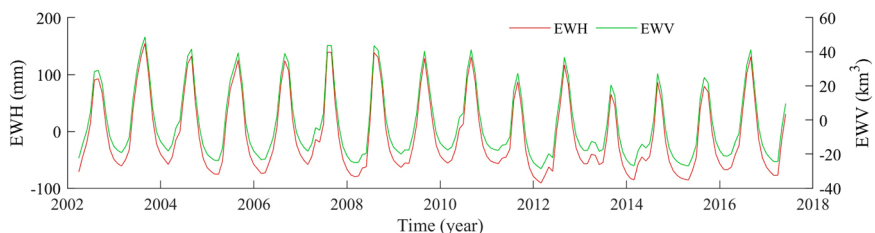


Fig. 8. Plot of TWCA time series. Red curve represents TWCA in EWH (mm) and green is EWW (km³).

Table 3. Notably, TWSA showed a significant trend of $\hat{\beta}_1 = 9.8$ ($s_{\hat{\beta}_1} = 0.8$) mm yr⁻¹.

4.6. Terrestrial Water Content (TWC) from GLDAS

Fig. 8 shows the TWCA time series. The peak TWCA (154.8 mm, 48.7 km³) occurred in September 2003 and the lowest (-90.9 mm, -28.6 km³) in March 2012. Contrary to GRACE, TWCA showed a declining trend of $\hat{\beta}_1 = 2.2$ ($s_{\hat{\beta}_1} = 0.4$) mm yr⁻¹ (**Table 3**).

4.7. The terrestrial water budget

We calculated three Δs time series: (1) $P - ET$ (net precipitation), (2) TWS change (TWSC) from GRACE (Eq. (3)), and (3) TWC change (TWCC) from GLDAS-Noah (Eq. (3)). **Fig. 9** shows these time series and $(P - ET)^f$ (filtered net P) – see **Section 3.2.1**. All but $(P - ET)^f$ showed no evidence of a trend (p-value > 0.05; **Table 3**).

We summarised their statistics in **Table 7**. All Δs time series were characterised by positive means, indicating that the UER received more water than it lost. The peak of net precipitation (288.9 mm mth⁻¹) occurred in August 2007 around the time of the anomalously high rainfall in the Volta Basin (see **Fig. 3**). Its maximum depletion (83.6 mm mth⁻¹) occurred around the start of the dry season in October 2007. TWSC peaked (139.4 mm mth⁻¹) in August 2015, with relatively smaller amplitudes than net P (**Fig. 9**), but the two time series were highly correlated ($r = 0.87$, p-value < 0.001). The minimum TWSC (-91.2 mm mth⁻¹) was recorded in November 2015. TWCC had comparatively smaller values.

The residual of filtered net P and TWSC ($\delta\Delta s_{\text{GRACE}}^f$) resulted in smaller differences than that of net P and TWSC (**Table 7**). Differences between net P and TWCC were the largest.

4.8. Meteorological conditions and water availability

The following describe the results of the relationships between water availability and the meteorological variables. **Fig. 10** shows the time series of humidity, pressure, SWR flux, temperature, and wind speed. All, except humidity, were characterised by increasing trends (**Table 8**).

The multiple r (**Section 3.2.5**) between P and the predictor variables was 0.88 (p-value < 0.0001). When we included ET in the predictor variables, we found no substantial change in r between P and the predictor variables (ET included). We also found similar relationships between ET and the predictor variables (with and without P). The percentages of the variations in P and ET that were explained by the predictor variables were similar, with multiple $R^2 = 0.76$ and 0.77 respectively. Thus, we conclude that our predictor variables had a similar influence on both ET and P .

Rainfall and ET had $r = 0.74$ (p-value < 0.001) and rainfall accounted for 54.0 % of the variations in ET . Cross-correlating P and ET showed that ET lagged rainfall by 1 mth, with maximum $r = 0.9$ (p-value < 0.001). This is equivalent to an $R^2 = 0.81$, suggesting that P accounted for 81 % of ET variations a month after rainfall. Hence, rainfall's maximum contribution to ET variations occurred a month after rainfall.

We analysed the ratio of ET to P , which is a measure of water surplus or deficit (**Castellani, 2017**). **Fig. 11** shows the resulting deficit/surplus graph. Ninety-three of the 183 months were characterised by a ratio < 1 (surplus). These surplus months were during the months of April to September in the years between 2002 and 2016 and April to June 2017. The average P in surplus months was 143.5 mm and average ET was 74.2 mm. Months of deficit ($\frac{ET}{P} > 1$) were between October and March, with average P of 15.8 mm and average ET of 42.7 mm. Both surplus and deficit months were equal in length, except in 2002 and 2017.

The multiple correlation analysis between TWSA and the predictor variables yielded an $R^2 = 0.3$ (p-value < 0.001). This value increased to $R^2 = 0.32$ and $R^2 = 0.65$ when P and ET were respectively added to the predictors (p-value < 0.001). The multiple $R^2 = 0.42$ when only P and ET were used as the predictor variables. However, ET and TWSA were more highly correlated ($r = 0.58$) than P and TWSA ($r = 0.22$). Nonetheless, cross-correlation analysis (**Section 3.2.4**) estimated a 2-month lag between P and TWSA ($r = 0.78$,

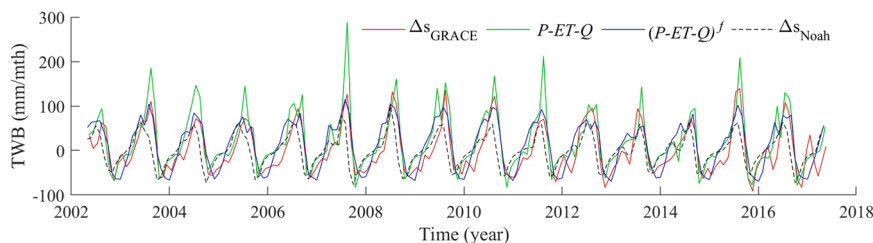


Fig. 9. Available water in the UER calculated as $P - ET$ (green) and calculated from GRACE (red) and GLDAS-Noah (black). The blue curve represents the time series of filtered net precipitation $(P - ET)^f$.

Table 7

Terrestrial water budget calculated from GRACE, GLDAS, and as full resolution and filtered net precipitation. Units: mm mth⁻¹; mm for Mean.

| Statistics | $P - ET$ | Δs_{GRACE} | Δs_{Noah} | $(P - ET)^f$ | $\delta \Delta s_{GRACE}$ | $\delta \Delta s_{Noah}$ | $\delta \Delta s_{GRACE}^f$ |
|------------|----------|--------------------|-------------------|--------------|---------------------------|--------------------------|-----------------------------|
| Min | -83.6 | -91.2 | -76.7 | -69.5 | -62.9 | -29.1 | -99.6 |
| Max | 288.9 | 139.4 | 100.4 | 115.1 | 162.1 | 225.7 | 80.4 |
| Mean | 21.8 | 0.71 | 0.36 | 11.8 | 21.0 | 21.4 | 11.1 |
| STD | 63.8 | 52.0 | 36.8 | 53.0 | 31.8 | 39.1 | 33.0 |

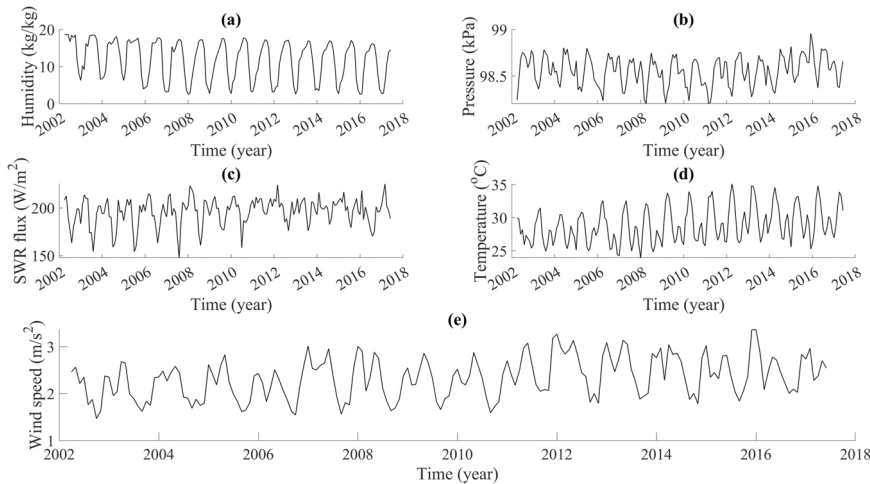


Fig. 10. Areal averages of (a) relative humidity, (b) pressure, (c) SWR flux, (d) temperature, and (e) wind speed.

Table 8

Harmonic analysis of the predictor variables showing the dimensionless constant term, the linear trend, the amplitudes and phases (°), and their standard errors. The standard errors are written in parentheses. Units: Humidity ($\hat{\beta}_1 = \text{kg kg}^{-1} \text{ yr}^{-1}$, $\hat{A} = \text{kg}$); Pressure ($\hat{\beta}_1 = \text{kPa yr}^{-1}$, $\hat{A} = \text{kPa}$); SWR ($\hat{\beta}_1 = \text{W m}^{-2} \text{ yr}^{-1}$, $\hat{A} = \text{W m}^{-2}$); Temperature ($\hat{\beta}_1 = \text{°C yr}^{-1}$, $\hat{A} = \text{°C}$); Wind speed ($\hat{\beta}_1 = \text{m s}^{-2} \text{ yr}^{-1}$, $\hat{A} = \text{m s}^{-2}$). O* represents p-value $\gg 0.05$ and O⁺ represents p-value = 0.06. All other parameters had p-value < 0.001 .

| Quantity | $\hat{\beta}_0$ | $\hat{\beta}_1$ (mm yr ⁻¹) | Amplitude | | Phase (°) | |
|-------------|-----------------|---|-------------|-------------|----------------|-------------------------|
| | | | \hat{A}_1 | \hat{A}_2 | $\hat{\phi}_1$ | $\hat{\phi}_2$ |
| Humidity | 11.7 (0.1) | -0.2 (0.03) | 6.7 (0.2) | 20.3 (1.4) | 2.0 (0.2) | 14.6 (4.6) |
| Pressure | 98.6 (0.01) | 0.003 (0.001) | 0.1 (0.01) | 15.5 (3.5) | 0.1 (0.01) | -3.3 (4.4)* |
| SWR | 195.7 (0.7) | 0.5 (0.2) | 13.9 (1.0) | 37.4 (3.9) | 7.8 (1.0) | -19.7 (7.0) |
| Temperature | 28.8 (0.1) | 0.2 (0.02) | 2.5 (0.1) | 30.8 (2.5) | 2.1 (0.1) | 18.5 (2.9) |
| Wind speed | 2.3 (0.02) | 0.03 (0.004) | 0.4 (0.03) | 33.1 (3.8) | 0.3 (0.03) | -8.0 (5.2) ⁺ |

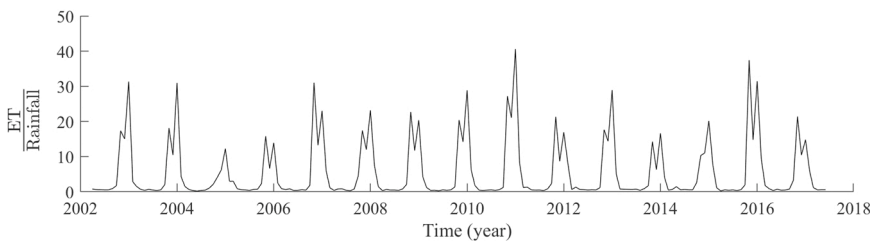


Fig. 11. Ratio of evapotranspiration to rainfall showing water deficit and surplus.

p-value < 0.001), with TWSA trailing P . This indicates that the maximum contribution of P to TWSA occurred after 2 months of rainfall.

TWCA was highly correlated with the predictor variables ($r = 0.89$, p-value < 0.001). Adding P to the predictor variables did not change the multiple r , but replacing P with ET increased the multiple r to 0.94 (p-value < 0.001). The multiple r when both ET and P were added to the predictor variables was around 0.94. The multiple r between P and ET as predictor variables and TWCA was 0.88 (p-

value < 0.001).

Net P compared well with the five predictor variables, yielding an $R^2 = 0.54$ (p-value < 0.001). P accounted for more than 90 % of the variation in net precipitation. Similarly, the R^2 between TWSC and the predictor variables was 0.64 (p-value < 0.001) and was higher when P was included in the predictor variables ($R^2 = 0.80$) than when ET was added ($R^2 = 0.64$). Collectively, ET , P , and the predictor variables explained a little over 80 % of the variations in TWSC, indicating a strong relationship between water availability and meteorological conditions. The multiple R^2 between TWCC, P , ET , and the predictor variables was 0.78 (p-value < 0.001). The R^2 between TWCC and the predictor variables was 0.48. This increased to 0.56 and 0.67 upon inclusion of ET and P , respectively, to the predictor variables.

5. Discussion

5.1. Intercomparison of solutions

The satellite- and gauge-based precipitation data sets were similar in their estimation of precipitation. This was evident in the closeness of their statistics (Table 4) and their high correlation coefficients. This is further supported by the statistics of their differences – maximum mean difference of around 12 mm (Table 4) – and by their σ_{TCH} . The ordering of the products based on their biases (Table 4) and σ_{TCH} may be explained by their constituent data. Recall that (1) CHIRPS combines satellite and gauge data (Funk et al., 2015), (2) GPM uses purely satellite data (Hou et al., 2014) and, (3) CPC uses purely gauge data (Xie et al., 2007, 2010). Combining gauge and satellite data can improve precipitation estimates. Conversely, the complete reliance on weather stations (CPC) could mean low data quality over data-poor regions such as the UER.

In contrast, the statistics of the differences between the ET data sets (Table 5) and their σ_{TCH} showed significant disparities between MOD16A2 and the other two solutions. MOD16A2 also underestimated ET by a relatively large amount (cf. Andam-Akorful et al., 2015). This observed behaviour of the MOD16A2 ET may be attributed to its forcing data, including MODIS land cover, leaf area index and meteorological data, which may be of low quality in regions like the UER (Mu et al., 2007, 2011). For instance, the coarse MODIS land cover used in MOD16A2 misclassifies the heterogeneity in savanna areas (Ramoelo et al., 2014) and could lead to biases (Chang et al., 2018) – e.g., the observed comparatively lower ET fluxes in the UER.

The GRACE solutions compared adequately well. Results of the intercomparison (Table 6) and σ_{TCH} analysis placed the mascon solutions ahead of the TELLUS land mass solution. This may point to the superiority of mascon regularisation techniques over the conventional processing techniques applied to GRACE L2 data. Another possibility is the use of newer data in the mascon solutions relative to the TELLUS grids.

5.2. Meteorology: P , ET and the predictors

The rainfall time series was characterised by no apparent temporal trend. This is in contrast to a related study over the UER that found a decreasing trend in rainfall (Issahaku et al., 2016). This difference in the findings between our study and Issahaku et al. (2016) could be because of the spatial distribution and resolution of the data sets. The latter studied rainfall from 6 gauge stations between 1954 and 2014.

The largest values of rainfall, which occurred in August, are consistent with Quaye-Ballard et al. (2020a). This is true not only for CHIRPS – Quaye-Ballard et al. (2020a) used CHIRPS in their study – but also for CPC and GPM. The peak P , recorded in August 2007 (Fig. 3), coincided with the anomalously high rainfall event which occurred in the same year in sub-Saharan Africa (Paeth et al., 2011). This anomaly was attributed to the 2007 La Niña, anomalies in atmospheric circulation, and the African easterly waves (Paeth et al., 2011).

The dry sub-humid classification from the aridity analysis indicated that the UER is prone to dryness (cf. Quaye-Ballard et al., 2020a). The trends of the predictor variables (Table 8) suggested they supported a drier climate and water loss through ET . However, considering the strong relationship between P and ET in the UER (cf. Rodell et al., 2011; Grippa et al., 2011; Andreini et al., 2000) and the similar effects of the predictors on P and ET , the trends of the predictor variables also support P .

5.3. Water storage and meteorological conditions

Our results showed contradictory trends between GRACE and GLDAS-Noah estimates of water storage. Possible explanations include (1) GRACE had a low SNR because of the area of the UER, thus leading to the observed increasing trend, (2) the unmodelled storage components in GLDAS-Noah contribute significantly to water storage in the UER, or (3) the water holding capacity of the soil in the UER. Items (2) and (3) both refer to GLDAS-Noah.

With regards to low GRACE SNR, the GRACE signals recovered over the UER included signals from the surrounding areas. If the signals had opposite signs or were substantially different, this would lead to a low SNR, making GRACE unusable over the UER. However, because the UER completely lies within the Volta Basin, we expect that the surrounding signals will not be different from the target. In the absence of in situ data, we used the water budget equation for validation. We see from Fig. 9 that GRACE TWSC and $P - ET$ were generally quite similar (cf. Ferreira and Zibrila, 2015) except when P was close to, or exceeded, ~ 300 mm mth^{-1} (discussed further in Section 5.4). One also sees that the differences became much smaller when net P was filtered to account for spectral inconsistencies (Fig. 9, Table 6). Although the UER is prone to dryness, a positive mean $P-ET$ value and $ET/P < 1$ for 51 % of the total months indicate that overall, the UER received more water through P than it lost through ET . These two metrics concur with

the observed increasing trend in TWSA. Our analysis has assumed that rainfall is the only input to the water cycle in the UER. However, given that there is no increasing rainfall trend, the TWSA trend is likely to have another source, such as the Bagre Dam, which floods the UER annually. We, however, did not have data to analyse its impact on TWSA.

We also found similarities between the annual amplitudes and linear trends of our study and that of [Ferreira et al. \(2012\)](#). Fig. 4 of [Ferreira et al. \(2012\)](#) shows the linear trend of GRACE in the UER to be between ~ 8 and 16 mm yr^{-1} . This is important because [Ferreira et al. \(2012\)](#) used GRACE level 2 data and their study was over the entire Volta Basin, the area of which is greater than twice the prescribed effective GRACE resolution ($150,000\text{--}200,000 \text{ km}^2$). Thus, based on our results and those of previous studies, we conclude that GRACE has a high SNR in the UER.

Concerning unmodelled storage components in GLDAS-Noah and the low water retention properties of the soil, TWCA in the UER comprises water stored in the soil and canopy ([Rui et al., 2018](#)). However, the total storage in a region comprises surface water, groundwater and any other major water storages. Canopy water storage made up only a small portion of TWCA perhaps because the region's vegetation is Savanna woodland. If there is substantial storage in the unmodelled components, this could result in GLDAS-Noah underestimating water storage. GRACE aggregates these distinct components vertically as TWSA, and because our results have established that GRACE can measure water storage in the UER, we conclude that soil moisture alone is not sufficient to describe the total water stored in the UER. Furthermore, if one considers the water retention properties of the soil in the UER, it becomes clear why modelled soil water can underestimate water storage in the UER. According to the [Ministry of Food and Agriculture \(2019\)](#), some of the soil in the UER has low water retention capacity. This claim is further supported by the global water capacity map ([United States Department of Agriculture, 2003](#)), which classified the UER's soil water capacity between low ($< 25 \text{ mm}$) and moderate ($25\text{--}100 \text{ mm}$). In light of this, and the statistics of ET/P and $P - ET$, we conclude that GLDAS underestimates water storage in the UER probably because of the unmodelled components and the dependence of TWCA on soil water.

Regarding the impact of meteorological conditions on water storage, the annual amplitude variations in rainfall could not entirely explain the annual amplitude variation in TWSA ($\hat{A}_1^P / \hat{A}_1^{\text{TWSA}} = 0.93$), implying that other factors (e.g., ET and other water inflow sources) contributed to \hat{A}_1^{TWSA} . This is to be expected because the UER has one season during which it receives water, but rainfall does not account for all the water in the UER ([Section 2.1](#)) or that it receives; and other processes (e.g., ET) in the dry season contribute to the annual amplitude variations. Conversely, rainfall alone was sufficient to explain \hat{A}_2^{TWSA} ($\hat{A}_2^P / \hat{A}_2^{\text{TWSA}} = 1.95$) probably because the impact of ET over the period was smaller than that of P , i.e., the UER received more water than it lost (see [Table 7](#) and [Section 4.8](#)).

5.4. Water availability

The positive mean values of all the Δs time series ([Table 7](#)) indicated that the UER received more water than it lost. The large difference between net P and Δs from GLDAS-Noah can be attributed to the lack of surface water in GLDAS-Noah ([Rui et al., 2018](#)) and perhaps the water retention properties of the soil in the UER ([Sections 2.1, 5.3; Ministry of Food and Agriculture, 2019](#)).

Two possible reasons for the difference between the GRACE Δs time series and net P are: (1) the 2-month lag between rainfall and the GRACE twin satellites sensing its maximum impact on the temporal variations of the gravity field (see [Section 4.8](#) and [Rieser et al., 2010](#)) and, (2) the spectral mismatch between GRACE and net precipitation. Notably, the wide variations between $P - ET$ and TWSC mainly resulted from their differences in August 2003, 2007, 2011, 2015 ([Fig. 9](#)). These periods coincided with rainfall exceeding 300 mm mth^{-1} . Given (1) the 2-month time lag between rainfall and GRACE, (2) that conditions (predictor variables) supported a drier climate and, (3) the strong relationship between ET and rainfall, it is probable that some of the water will have been lost through ET . Runoff had little to no effect on water loss, since it did not exceed 2 mm mth^{-1} . Notwithstanding, the differences between net P and GRACE TWSC were smaller than the bias of net P and TWCC. Filtering $P - ET$ lowered the differences between filtered net P and TWSC. Furthermore, similarities between our study and that of [Andam-Akorful et al. \(2015\)](#) provide additional support for the usability of GRACE over the UER. Most importantly, based on our water budget analysis, one would require a mean of 21.0 mm of TWSC to close the water budget of the UER using GRACE between 2002 and 2017. This translates roughly into a correction of 0.11 mm mth^{-1} to close the UER's water budget. Thus, we conclude that the SNR of GRACE in the UER is high, and GRACE can provide information for water resources monitoring in the region.

5.5. Limitations and recommendations

The main limitation of this study was the unavailability of in situ data. For instance, we did not have the necessary data to analyse the impact of the Bagre Dam on water resources in the UER. Given that TWSA was increasing while rainfall showed no trend, information from the Bagre Dam could improve the understanding of TWSA dynamics in the UER, especially the observed $9.8 \pm 0.8 \text{ mm yr}^{-1}$ trend. This can be important to the authorities of the yet to be constructed Pwalugu Dam. A future study could analyse the contribution of the Bagre Dam to determine its contribution to the increasing TWSA trend.

6. Conclusions

We assessed globally available hydro-meteorological data to study the impact of the climate of the UER on its water resources. We validated the GRACE and GLDAS water storage time series using the water budget equation and found large differences between net precipitation and GLDAS-Noah. The GRACE solution however compared well with net precipitation except when rainfall exceeded

300 mm mth⁻¹. These results indicated that GRACE can provide support for water resources monitoring in the UER. Our results also showed that conditions in the UER affect *P* and *ET* in a similar way, but that overall, the UER received more water through *P* than it lost through *ET*. All the time series of net *P*, an indication of water availability, were characterised by positive means. Water storage from GRACE showed an increasing trend of $9.8 \pm 0.8 \text{ mm yr}^{-1}$, which likely includes the contribution of another source of water (the Bagre Dam) other than rainfall.

Declaration of Competing Interest

The authors declare that they have no known competing financial interests or personal relationships that could have appeared to influence the work reported in this paper.

Acknowledgement

This research was supported by a Faculty of Science and Engineering Ph.D. scholarship, reference code 19073FOSE, to C.I. Kelly at the University of Nottingham Ningbo China, Ningbo, China.

References

- Abdi, H., 2007. Multiple correlation coefficient. *Encyclopedia of Measurement and Statistics*, p. 651.
- Abolafia-Rosenzweig, R., Pan, M., Zeng, J., Livneh, B., 2021. Remotely sensed ensembles of the terrestrial water budget over major global river basins: an assessment of three closure techniques. *Remote Sens. Environ.* 252, 112191.
- Andam-Akorful, S., Ferreira, V.G., Awange, J.L., Forootan, E., He, X., 2015. Multi-model and multi-sensor estimations of evapotranspiration over the Volta Basin, West Africa. *Int. J. Climatol.* 35, 3132–3145.
- Andreini, M., Giesen, N., Edig, A., Fosu, M., Andah, W., 2000. Volta Basin Water Balance. Technical Report. ZEF discussion papers on development policy.
- Bempah, S.A., Oyhus, A.O., 2017. The role of social perception in disaster risk reduction: beliefs, perception, and attitudes regarding flood disasters in communities along the Volta River, Ghana. *Int. J. Disaster Risk Reduct.* 23, 104–108.
- Biancamaria, S., Mballo, M., Le Moigne, P., Pérez, J.M.S., Espitalier-Noël, G., Grusson, Y., Cakir, R., Häfliger, V., Barathieu, F., Trasmonte, M., et al., 2019. Total water storage variability from GRACE mission and hydrological models for a 50,000 km² temperate watershed: the Garonne River basin (France). *J. Hydrol.: Reg. Stud.* 24, 100609.
- Brutsaert, W., 2005. *Hydrology: An Introduction*. Cambridge University Press, Cambridge.
- Castellani, B., 2017. Precipitation vs. evaporation: Colorado's losing battle. (<https://www.bouldercast.com/fighting-a-losing-battle-precipitation-vs-evaporation/>), (Accessed 25 May 2021).
- Chang, Y., Qin, D., Ding, Y., Zhao, Q., Zhang, S., 2018. A modified MOD16 algorithm to estimate evapotranspiration over alpine meadow on the Tibetan Plateau, China. *J. Hydrol.* 561, 16–30.
- Chatfield, C., Xing, H., 2019. Bivariate processes. In: *The Analysis of Time Series: An Introduction with R*, 7 ed. Chapman and Hall/CRC, pp. 199–215.
- Chen, J.L., Wilson, C.R., Tapley, B.D., 2010. The 2009 exceptional Amazon flood and interannual terrestrial water storage change observed by GRACE. *Water Resour. Res.* 46.
- Cherlet, M., Hutchinson, C., Reynolds, J., Hill, J., Sommer, S., von Maltitz, G., 2018. *World Atlas of Desertification*. Publication Office of the European Union, Luxembourg.
- Christensen, J.H., Kanikicharla, K.K., Aldrian, E., An, S.I., Cavalcanti, I.F.A., de Castro, M., Dong, W., Goswami, P., Hall, A., Kanyanga, J.K., et al., 2013. Climate phenomena and their relevance for future regional climate change. In: *Climate Change 2013 The Physical Science Basis: Working Group I Contribution to the Fifth Assessment Report of the Intergovernmental Panel on Climate Change*. Cambridge University Press, pp. 1217–1308.
- Ferreira, V.G., Gong, Z., Andam-Akorful, S.A., 2012. Monitoring mass changes in the Volta River basin using GRACE satellite gravity and TRMM precipitation. *Bol. Ciênc. Geod.* 18, 549–563.
- Ferreira, V.G., Montecino, H.D., Yakubu, C.I., Heck, B., 2016. Uncertainties of the gravity recovery and climate experiment time-variable gravity-field solutions based on three-cornered hat method. *J. Appl. Remote Sens.* 10, 015015.
- Ferreira, V.G., Zibrila, A., 2015. An investigation on the closure of the water budget methods over Volta Basin using multi-satellite data. In: *IGFS 2014*. Springer, pp. 171–178.
- Funk, C., Peterson, P., Landsfeld, M., Pedreros, D., Verdin, J., Shukla, S., Husak, G., Rowland, J., Harrison, L., Hoell, A., et al., 2015. The climate hazards infrared precipitation with stations—a new environmental record for monitoring extremes. *Sci. Data* 2, 1–21.
- Galindo, F.J., Palacio, J., 2003. Post-processing ROA data clocks for optimal stability in the ensemble timescale. *Metrologia* 40, S237.
- Ghana Statistical Service, 2014. 2010 Population & housing census. District analytical report: Nabdum District. (https://www2.statsghana.gov.gh/docfiles/2010_District_Report/Upper%20East/NABDAM.pdf), (Accessed 6 June 2021).
- Ghana Web, 2021. Pwalugu multi-purpose dam and irrigation project will be soul saving. (<https://www.ghanaweb.com/GhanaHomePage/NewsArchive/Pwalugu-Multi-Purpose-Dam-and-Irrigation-Project-will-be-Soul-Saving-1197379>), (Accessed 15 May 2021).
- Gray, J.E., Allan, D.W., 1974. A method for estimating the frequency stability of an individual oscillator. In: *Proceedings of the 28th Annual Symposium on Frequency Control*. IEEE, pp. 243–6.
- Grippa, M., Kergoat, L., Frappart, F., Araud, Q., Boone, A., De Rosnay, P., Lemoine, J.M., Gascoïn, S., Balsamo, G., Otle, C., et al., 2011. Land water storage variability over West Africa estimated by Gravity Recovery and Climate Experiment (GRACE) and land surface models. *Water Resour. Res.* 47.
- Guo, J., Zhou, L., Yao, C., Hu, J., 2016. Surface subsidence analysis by multi-temporal InSAR and GRACE: a case study in Beijing. *Sensors* 16, 1495.
- Harris, I., Osborn, T.J., Jones, P., Lister, D., 2020. Version 4 of the CRU TS monthly high-resolution gridded multivariate climate dataset. *Sci. Data* 7, 1–18.
- Hersbach, H., de Rosnay, P., Bell, B., Schepers, D., Simmons, A., Soci, C., Abdalla, S., Alonso-Balmaseda, M., Balsamo, G., Bechtold, P., et al., 2018. Operational global reanalysis: progress, future directions and synergies with NWP (<https://www.ecmwf.int/node/18765>), (<https://doi.org/10.21957/tkic6g3wm>).
- Hou, A.Y., Kakar, R.K., Neeck, S., Azarbarzin, A.A., Kummerow, C.D., Kojima, M., Oki, R., Nakamura, K., Iguchi, T., 2014. The global precipitation measurement mission. *Bull. Am. Meteorol. Soc.* 95, 701–722.
- Issahaku, A.R., Campion, B.B., Edziyie, R., 2016. Rainfall and temperature changes and variability in the Upper East Region of Ghana. *Earth Space Sci.* 3, 284–294.
- Kelly, C., Andam-Akorful, S., Hancock, C., Laari, P., Ayer, J., 2021. Global gravity models and the Ghanaian Vertical Datum: challenges of a proper definition. *Surv. Rev.* 53, 44–54.
- Kutner, M.H., Nachtsheim, C.J., Neter, J., Li, W., et al., 2005. *Applied Linear Statistical Models*, 5 ed. McGraw-Hill, New York.
- Landerer, F., 2020. TELLUS GRAC_L3_CSR_RL06_LND_v03. Ver. RL06 v03. PO.DAAC, CA, USA. (<https://doi.org/10.5067/TELND-3AC63>), (Accessed 2 February 2021).
- Landerer, F.W., Flechtner, F.M., Save, H., Webb, F.H., Bandikova, T., Bertiger, W.I., Bettadpur, S.V., Byun, S.H., Dahle, C., Dobslaw, H., et al., 2020. Extending the global mass change data record: GRACE follow-on instrument and science data performance. *Geophys. Res. Lett.* 47, e2020GL088306.
- Landerer, F.W., Swenson, S., 2012. Accuracy of scaled GRACE terrestrial water storage estimates. *Water Resour. Res.* 48.

- Longuevergne, L., Wilson, C., Scanlon, B., Crétaux, J., 2013. GRACE water storage estimates for the Middle East and other regions with significant reservoir and lake storage. *Hydrol. Earth Syst. Sci.* 17, 4817–4830.
- McColl, K.A., Vogelzang, J., Konings, A.G., Entekhabi, D., Piles, M., Stoffelen, A., 2014. Extended triple collocation: estimating errors and correlation coefficients with respect to an unknown target. *Geophys. Res. Lett.* 41, 6229–6236.
- Ministry of Food and Agriculture, 2019. Upper East Region. (<http://mofa.gov.gh/site/directorates/regional-directorates/upper-east-region/>), (Accessed 6 June 2021).
- Mu, Q., Heinsch, F.A., Zhao, M., Running, S.W., 2007. Development of a global evapotranspiration algorithm based on MODIS and global meteorology data. *Remote Sens. Environ.* 111, 519–536.
- Mu, Q., Zhao, M., Running, S.W., 2011. Improvements to a MODIS global terrestrial evapotranspiration algorithm. *Remote Sens. Environ.* 115, 1781–1800.
- Ni, S., Chen, J., Wilson, C.R., Hu, X., 2017. Long-term water storage changes of Lake Volta from GRACE and satellite altimetry and connections with regional climate. *Remote Sens.* 9, 842.
- Ogawa, R., Chao, B.F., Heki, K., 2011. Acceleration signal in grace time-variable gravity in relation to interannual hydrological changes. *Geophys. J. Int.* 184, 673–679.
- Owusu, A.B., Cervone, G., Luzzadder-Beach, S., 2013. Analysis of desertification in the Upper East Region (UER) of Ghana using remote sensing, field study, and local knowledge. *Cartogr.: Int. J. Geogr. Inform. Geovisual.* 48, 22–37.
- Paeth, H., Fink, A.H., Pohle, S., Keis, F., Mächel, H., Samimi, C., 2011. Meteorological characteristics and potential causes of the 2007 flood in sub-Saharan Africa. *Int. J. Climatol.* 31, 1908–1926.
- Premoli, A., Tavella, P., 1993. A revisited three-cornered hat method for estimating frequency standard instability. *IEEE Trans. Instrum. Meas.* 42, 7–13.
- Quaye-Ballard, J., Okrah, T., Andam-Akorful, S., Awotwi, A., Antwi, T., Osei-Wusu, W., Tang, X., Quaye-Ballard, N., 2020a. Spatiotemporal dynamics of rainfall in Upper East Region of Ghana, West Africa, 1981–2016. *SN Appl. Sci.* 2, 1–12.
- Quaye-Ballard, J., Okrah, T., Andam-Akorful, S., Awotwi, A., Osei-Wusu, W., Antwi, T., Tang, X., 2020b. Assessment of vegetation dynamics in Upper East Region of Ghana based on wavelet multi-resolution analysis. *Model. Earth Syst. Environ.* 6, 1783–1793.
- Ramillien, G., Frappart, F., Günter, A., Ngo-Duc, T., Cazenave, A., Laval, K., 2006. Time variations of the regional evapotranspiration rate from Gravity Recovery and Climate Experiment (GRACE) satellite gravimetry. *Water Resour. Res.* 42.
- Ramoelo, A., Majazi, N., Mathieu, R., Jovanovic, N., Nickless, A., Dziki, S., 2014. Validation of global evapotranspiration product (MOD16) using flux tower data in the African savanna, South Africa. *Remote Sens.* 6, 7406–7423.
- Riegger, J., Tourian, M., Devaraju, B., Sneeuw, N., 2012. Analysis of GRACE uncertainties by hydrological and hydro-meteorological observations. *J. Geodyn.* 59, 16–27.
- Rieser, D., Kuhn, M., Pail, R., Anjasmara, I., Awange, J., 2010. Relation between grace-derived surface mass variations and precipitation over australia. *Aust. J. Earth Sci.* 57, 887–900.
- Rodell, M., Famiglietti, J., Chen, J., Seneviratne, S., Viterbo, P., Holl, S., Wilson, C., 2004a. Basin scale estimates of evapotranspiration using GRACE and other observations. *Geophys. Res. Lett.* 31.
- Rodell, M., Houser, P., Jambor, U., Gottschalck, J., Mitchell, K., Meng, C.J., Arsenault, K., Cosgrove, B., Radakovich, J., Bosilovich, M., et al., 2004b. The global land data assimilation system. *Bull. Am. Meteorol. Soc.* 85, 381–394.
- Rodell, M., McWilliams, E.B., Famiglietti, J.S., Beaudoing, H.K., Nigro, J., 2011. Estimating evapotranspiration using an observation based terrestrial water budget. *Hydrol. Process.* 25, 4082–4092.
- Rowlands, D.D., Luthcke, S., Klosko, S., Lemoine, F.G., Chinn, D., McCarthy, J., Cox, C., Anderson, O., 2005. Resolving mass flux at high spatial and temporal resolution using GRACE intersatellite measurements. *Geophys. Res. Lett.* 32.
- Rui, H., Beaudoing, H., Loeser, C., 2018. README Document for NASA GLDAS Version 2 Data Products. Goddard Earth Sciences Data and Information Services Center (GES DISC), Greenbelt, MD, USA.
- Save, H., 2020. CSR GRACE and GRACE-FO RL06 Mascon Solutions v02. (http://www2.csr.utexas.edu/grace/RL06_mascons.html), (<https://doi.org/10.15781/cgq9-nh24>), 2020. (Accessed 1 January 2020).
- Save, H., Bettadpur, S., Tapley, B.D., 2016. High-resolution CSR GRACE RL05 mascons. *J. Geophys. Res.: Solid Earth* 121, 7547–7569.
- Syed, T.H., Famiglietti, J.S., Rodell, M., Chen, J., Wilson, C.R., 2008. Analysis of terrestrial water storage changes from GRACE and GLDAS. *Water Resour. Res.* 44.
- Tavella, P., Premoli, A., 1994. Estimating the instabilities of N clocks by measuring differences of their readings. *Metrologia* 30, 479.
- Tourian, M., Elmi, O., Chen, Q., Devaraju, B., Roohi, S., Sneeuw, N., 2015. A spaceborne multisensor approach to monitor the desiccation of Lake Urmia in Iran. *Remote Sens. Environ.* 156, 349–360.
- United States Department of Agriculture, 2003. Assessment of water holding capacity of soils map. (https://www.nrcs.usda.gov/wps/portal/nrcs/detail/soils/use/?cid=nrcs142p2_054022), (Accessed 28 May 2022).
- Vishwakarma, B.D., Devaraju, B., Sneeuw, N., 2018. What is the spatial resolution of GRACE satellite products for hydrology? *Remote Sens.* 10, 852.
- Wahr, J., Molenaar, M., Bryan, F., 1998. Time variability of the Earth's gravity field: hydrological and oceanic effects and their possible detection using GRACE. *J. Geophys. Res.: Solid Earth* 103, 30205–30229.
- Wahr, J., Swenson, S., Zlotnicki, V., Velicogna, I., 2004. Time-variable gravity from GRACE: first results. *Geophys. Res. Lett.* 31.
- Wiese, D.N., Landerer, F.W., Watkins, M.M., 2016. Quantifying and reducing leakage errors in the JPL RL05M GRACE mascon solution. *Water Resour. Res.* 52, 7490–7502.
- Wiese, D.N., Yuan, D.N., Boening, C., Landerer, F.W., Watkins, M.M., 2019. JPL GRACE Mascon Ocean, Ice, and Hydrology Equivalent Water Height RL06 CRI Filtered Version 02. Ver. 02. PO.DAAC, CA, USA. (<https://doi.org/10.5067/TEMSC-3JC62>), (Accessed 23 January 2021).
- World Meteorological Organization, 2020. State of the global climate 2020. (<https://public.wmo.int/en/our-mandate/climate/wmo-statement-state-of-global-climate>).
- Xie, P., Chen, M., Shi, W., 2010. CPC unified gauge-based analysis of global daily precipitation. In: Preprints, 24th Conf. on Hydrology, Atlanta, GA, Amer. Meteor. Soc.
- Xie, P., Chen, M., Yang, S., Yatagai, A., Hayasaka, T., Fukushima, Y., Liu, C., 2007. A gauge-based analysis of daily precipitation over East Asia. *J. Hydrometeorol.* 8, 607–626.
- Yakubu, C.I., Ayer, J., Laari, P.B., Amponsah, T.Y., Hancock, C.M., 2019. A mutual assessment of the uncertainties of digital elevation models using the triple collocation technique. *Int. J. Remote Sens.* 40, 5301–5314.
- Yiran, G.A., Stringer, L.C., 2016. Spatio-temporal analyses of impacts of multiple climatic hazards in a savannah ecosystem of Ghana. *Clim. Risk Manag.* 14, 11–26.
- Zheng, M., Deng, K., Fan, H., Du, S., 2018. Monitoring and analysis of surface deformation in mining area based on InSAR and GRACE. *Remote Sens.* 10, 1392.